

UNCLASSIFIED

Defense Technical Information Center  
Compilation Part Notice

ADP023694

TITLE: Thermal Lensing in the Ocular Media

DISTRIBUTION: Approved for public release, distribution unlimited

This paper is part of the following report:

TITLE: Conference on Optical Interactions with Tissue and Cells [18th]  
Held in San Jose, California on January 22-24, 2007

To order the complete compilation report, use: ADA484275

The component part is provided here to allow users access to individually authored sections of proceedings, annals, symposia, etc. However, the component should be considered within the context of the overall compilation report and not as a stand-alone technical report.

The following component part numbers comprise the compilation report:

ADP023676 thru ADP023710

UNCLASSIFIED

# Thermal lensing in the ocular media.

Rebecca L. Vincelette<sup>a,b</sup>, Robert J. Thomas<sup>a</sup>, Benjamin A. Rockwell<sup>a</sup>, Ashley J. Welch<sup>b</sup>

<sup>a</sup>USAF Research Laboratory, 2624 Louis Bauer Dr., Brooks City-Base, TX, 78235-5278

<sup>b</sup>University of Texas in Austin, Department of Biomedical Engineering, 1 University Station C0800, Austin, TX, 78712

## ABSTRACT

A tissue phantom of water with an absorbing dye, Allura Red, was used to observe the effects of thermal lensing in a thick sample exposed to a CW 532 nm Verdi laser. A collimated beam was sent through a sample 2.9 cm thick. Results from the collimated beam revealed qualitative information about thermal lensing in a liquid media. The studies presented here argue the relevance of incorporating oscillating factors such as convectional flow into higher order thermal lensing models in a fluid such as water.

**Keywords:** Thermal Lensing, Artificial Eye, Optical Radiation, Tissue Phantom, Ocular Media, Laser Eye Safety

## 1. INTRODUCTION

Predicting complete laser-tissue effects in an ocular exposure are important for modeling damage processes at the retina to provide fundamental understandings of the mechanisms involved in a damage process. Such understandings provide key information for balancing safety and technological efficacy for intentional or unintentional laser eye exposures.

Spot size at the retina is a prime contributor in determining the damage threshold at the retina.<sup>[1]</sup> Thus, accurately predicting spot size is crucial to modeling damage at the retina. Physical changes resulting from a laser exposure within a homogeneous media such as the vitreous humor can alter a beam's minimum waist position or size. When spot sizes are a few 100  $\mu\text{m}$  or less, a 50  $\mu\text{m}$  variation in spot size could mean a large impact on the presence or absence of a lesion on the retina.

Thermal lensing is a physical phenomenon arising from the temperature increase as photons are absorbed throughout a media.<sup>[2]</sup> As the temperature rises, two physical changes occur in a liquid media. First the density,  $\rho$ , of the molecules decreases as temperature increases and secondly, the local index of refraction,  $n$ , decreases. The Gaussian radial profile of the laser beam creates a negative temperature gradient in the radial direction causing a slight divergence of the collimated or focused beam. Thermal lensing has been studied extensively in solid state optics, but remains largely ill-represented in optically thick samples which are highly absorbing and possibly scattering such as biological tissues. Of course the presence of thermal lensing is strongly dependent upon the absorption of energy, thus a threshold of thermal lensing effect must exist where it is strong and weak. As a result, wavelengths in the near infrared, NIR, are of particular interest for thermal lensing studies.

Previously presented thermal lensing models only considered first-order effects for thinner samples in a controlled z-scan setting.<sup>[3,4]</sup> One of the long term goals in this research is to develop a thermal lensing model for the human eye. In order to successfully model this complicated process, the physical characteristics and influential parameters need to be understood and quantified. In this study, a tissue phantom created from water and a 532 nm absorber were used to observe changes in beam diameter as a function of time using a high speed camera. Qualitative assessments of the beam's changes were derived from the video data.

## 2. METHODOLOGY

### 2.1 Tissue phantom development

The linear absorption coefficient,  $\mu_a$ , in the NIR has been measured by Maher et al. and compared to the absorption of water by Hale et al.<sup>[5, 6]</sup> Clearly, water serves as an excellent tissue phantom to approximate the absorbance of these tissues in the NIR.

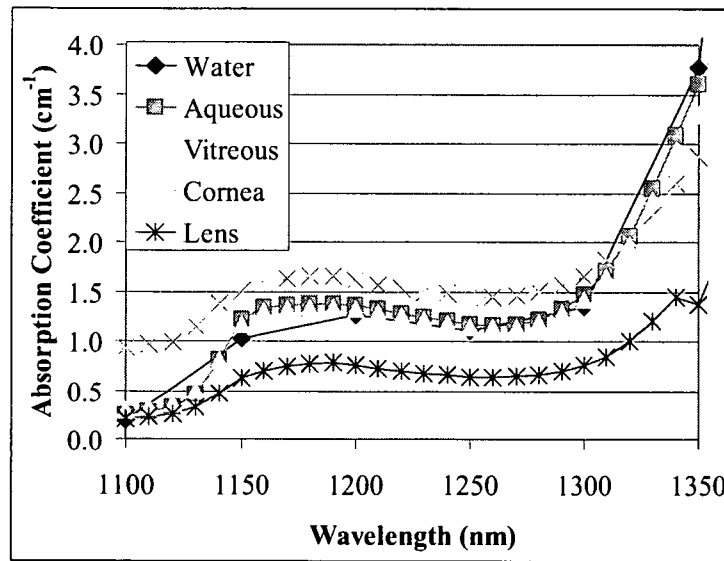


Fig. 1: Linear absorption coefficient,  $\mu_a$ , as a function of wavelength for ocular media compared to water.<sup>[5, 6]</sup>

Variability in the exact absorption of NIR for water is reported from several sources in Fig. 2 below.<sup>[5, 7-11]</sup> This Figure illustrates an approximation on the tolerance of allowable absorbance in the NIR region between 1100-1350 nm.

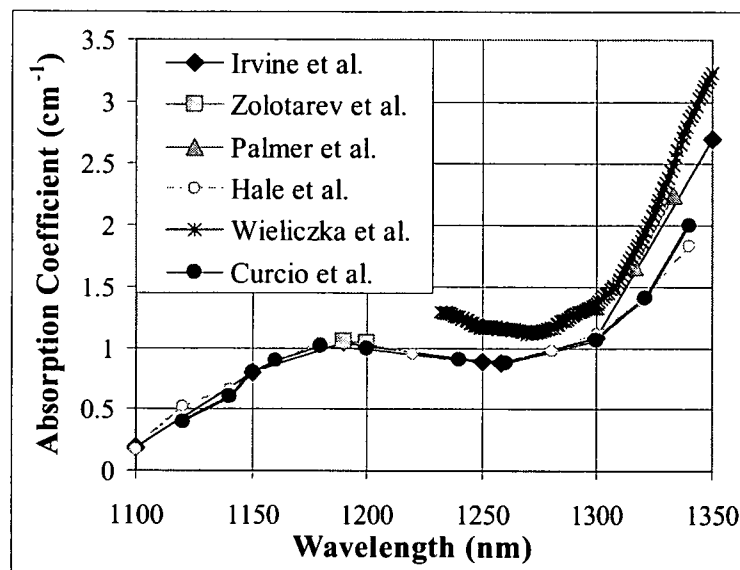


Fig. 2: Comparison of reported absorption coefficients for pure water in the NIR.<sup>[5, 7-11]</sup>

At 1100 nm, the absorption coefficient is approximately  $0.25 \text{ cm}^{-1}$ , but begins to climb to a plateau around  $1.00 \text{ cm}^{-1}$  in the 1200 nm region. At 1300 nm, the absorption coefficient begins to climb again, though more steeply than in the 1100 nm region. Over the 1100 – 1350 nm region in regards to ocular tissue spectra shown in Fig. 1, the cornea remains higher than water, aqueous, vitreous and lens until approximately 1300 nm. The reverse is true for the lens tissue, where the absorption coefficient remains lower than water, vitreous, aqueous and cornea after 1125 nm through 1150 nm. In all ocular tissues over this NIR range, water exhibits similar trends in absorbance over this wavelength region. As a result, a

tissue phantom with an easily controlled absorbance would be advantageous to investigate the thermal lensing effect to simulate a wide range of wavelengths to approximate a variety of tissue responses using a single laser source.

Unfortunately, imaging in the NIR can be monetarily expensive. A tissue phantom was developed on the pretense of water having an absorption coefficient near  $1.80 \text{ cm}^{-1}$  at 1315 nm using Allura Red dye. The purpose of the phantom was to create a higher absorption coefficient of water at a visible wavelength for the purposes of imaging with a high speed visible camera. An available 532 nm Verdi laser was used for all CW exposures. A stock solution of Allura Red was created from 91% pure dye from Spectrum Chemicals Mfg. Sample concentrations of aqueous  $4.88 \cdot 10^{-5}$ ,  $7.32 \cdot 10^{-5}$  and  $9.76 \cdot 10^{-5}$  M dye were created for the experiment. All samples were kept at room temperature of approximately  $21^\circ\text{C}$  and kept air tight for storage. Each dye concentration was placed in a 1 cm quartz cuvette to determine the linear absorption coefficient using Beer's Law.

## 2.2 Imaging

A collimated beam was sent through an artificial eye with plastic window inserts, refer to schematics below. An 818-SL Newport detector and 1830-C Newport Power Meter were used to measure the power immediately before and after the sample. A Photron™ Superfast Cam 10k by was used to image the beam on a screen two meters behind the sample at a frame rate of 250 fps. Neutral density filters were used just before the imaging screen to cut back on pixel saturation when necessary.

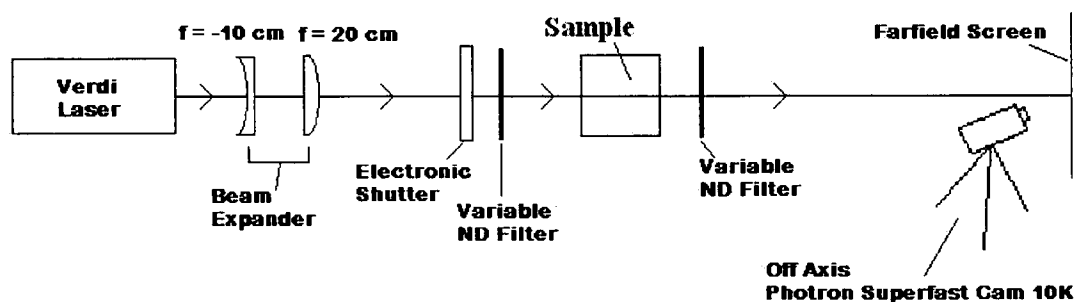


Fig. 3: Schematic of optical configuration. Initial attempts to image at the focal plane of a fast lens yielded inconclusive results with poor signal to noise. Though imaging the transient response of the beam waist at the focal plane is ideal, the focusing lens was removed and a collimated beam was passed through the sample then imaged in the farfield.

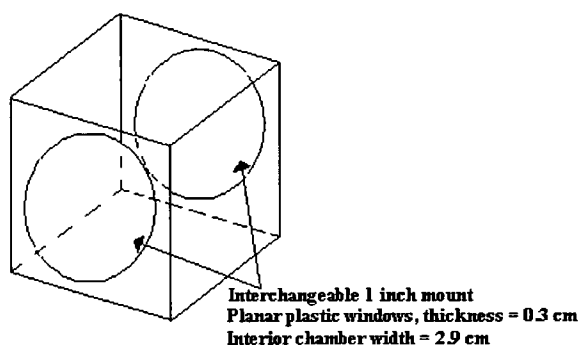


Fig. 4: Schematic of the sample cell, or Cain cell.<sup>[12]</sup> No focusing lenses were used in the data collection presented in this paper. All cell windows consisted of plastic disk inserts approximately 0.3 cm thick.

Using a knife edge technique, the beam divergence after the beam expander was measured to be  $29.5 \mu\text{rad}$  with a  $1/e^2$  beam radius of about 3 mm at the sample. A sample of pure water was imaged initially at powers up to 430 mW to determine any changes in beam shape due to water alone at 532 nm. Then samples of various dye concentrations were placed in the artificial eye. Each sample was then exposed to the 532 nm laser with the electronic shutter and recorded by the camera triggered off a Stanford Research Systems Signal Generator model DG535. The video files were recorded at a rate of 250 fps. All video files were transferred into individual frames for analysis in MATLAB.

### 3. DATA & RESULTS

Table 1: Dye concentrations and corresponding linear absorption coefficients from Beer's Law using a 1 cm quartz cuvette. Approximate correlating wavelengths from Fig. 2 are 1250-1300, 1310-1320, and 1320-1340 nm for the solutions with absorption coefficients of 0.95, 1.37 and 1.80  $\text{cm}^{-1}$  respectively.

[Allura Red] (M)	$P_{in}$ (mW)	$P_{out}$ (mW)	$\mu_a$ (1/cm)
$4.88 \cdot 10^{-5}$	47.6	5.3	0.953
$7.32 \cdot 10^{-5}$	47.83	2.04	1.370
$9.76 \cdot 10^{-5}$	48.7	0.77	1.801

Experiments 1 and 2 from Table 2 did not yield any definitive changes in the 532 nm beam's shape in the far-field, though some losses were evident. Losses were attributed to absorption, reflectance and scattering of the planar plastic plates. The linear absorption coefficient of pure water at 532 nm is approximately  $4.4 \cdot 10^{-4} \text{ cm}^{-1}$  as reported by Hale et al.<sup>[5]</sup> To adjust for these losses, the average raw transmission from experiments 1 and 2 was 92.737 % which was then used to normalize all remaining experiments.

Table 2: Power delivered to samples of dye concentrations used in this study. The first two samples were pure water.

Experiment	$\mu_a$ (Table 1) ( $\text{cm}^{-1}$ )	Power (mW)		% Raw Transmission	% Normalized Transmission
		Before Art. Eye	After Art. Eye		
1	$4.4 \cdot 10^{-4}$	128	118	92.188	100
2	$4.4 \cdot 10^{-4}$	430	398	92.558	100
3	0.95	128	0.219	0.171	0.185
4	0.95	434	0.697	0.161	0.174
5	1.37	320	0.0518	0.016	0.018
6	1.37	615	0.078	0.013	0.014
7	1.80	128	0.0233	0.018	0.020

Experiments 3 and 4 depicted in Fig. 5 correspond to cases of absorption in the 1250 – 1300 nm regions from Fig. 2 where the absorption coefficient measured in a 1 cm cuvette was found to be  $0.95 \text{ cm}^{-1}$  as reported in Table 1. In Experiment 3, the beam began to gradually spread out, forming a crescent shape as the upper portion of the beam disappeared. To the naked eye, the beam appeared to shift in intensity with the lower portion becoming brighter after several seconds. For Experiment 4, the beam appeared symmetrical initially, but as it spread out, the center melted away forming a crescent.

Experiments 5 and 6 depicted in Fig. 6 correspond to cases of absorption in the 1310 – 1320 nm regions from Fig. 2 where the absorption coefficient measured in a 1 cm cuvette was found to be  $1.37 \text{ cm}^{-1}$  as reported in Table 1. In Experiments 5 and 6, a crescent effect was observed where the magnitude and appearance of the crescent were related to the power delivered to the sample. The crescent shape also appeared more rapidly in the higher concentration and even more so for higher power cases. In Experiment 6 an oscillation was observed in the crescent state where the slivered shape appeared to expand and contract on a shallow, though obvious, scale. This oscillation is suspected to be directly related to convectional flow.

Experiment 7, the case with the highest concentration, corresponds to cases of absorption in the 1320 – 1340 nm regions from Fig. 2 where the absorption coefficient measured in a 1 cm cuvette was found to be  $1.80 \text{ cm}^{-1}$  as reported in Table 1. In Experiment 7, the beam could not be captured with the camera though it was observable with the naked eye. The beam appeared to be more spread out in the far-field compared to the other Experiments, causing the signal to dip just

into the noise level of the camera rendering any image collection to be very difficult. The donut shape was seen along with the oscillating crescent where the rate of the oscillation was higher than Experiment 6. The power was taken as high as 1.25 W and the event still remained too low an intensity for the camera to capture.

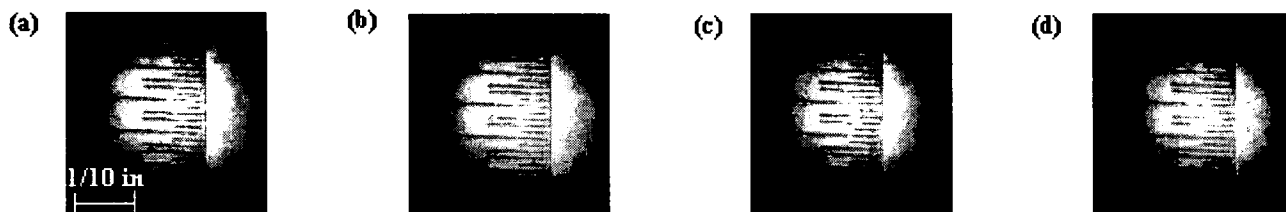


Fig. 5: Results from water blanks (no dye). Experiment 1 from Table 2 at 0 sec (a) and 5 sec (b). Experiment 2 from Table 2 at 0 sec (c) and 5 sec (d). The ruler was placed at the image plane for calibration. Each division is 1/100".

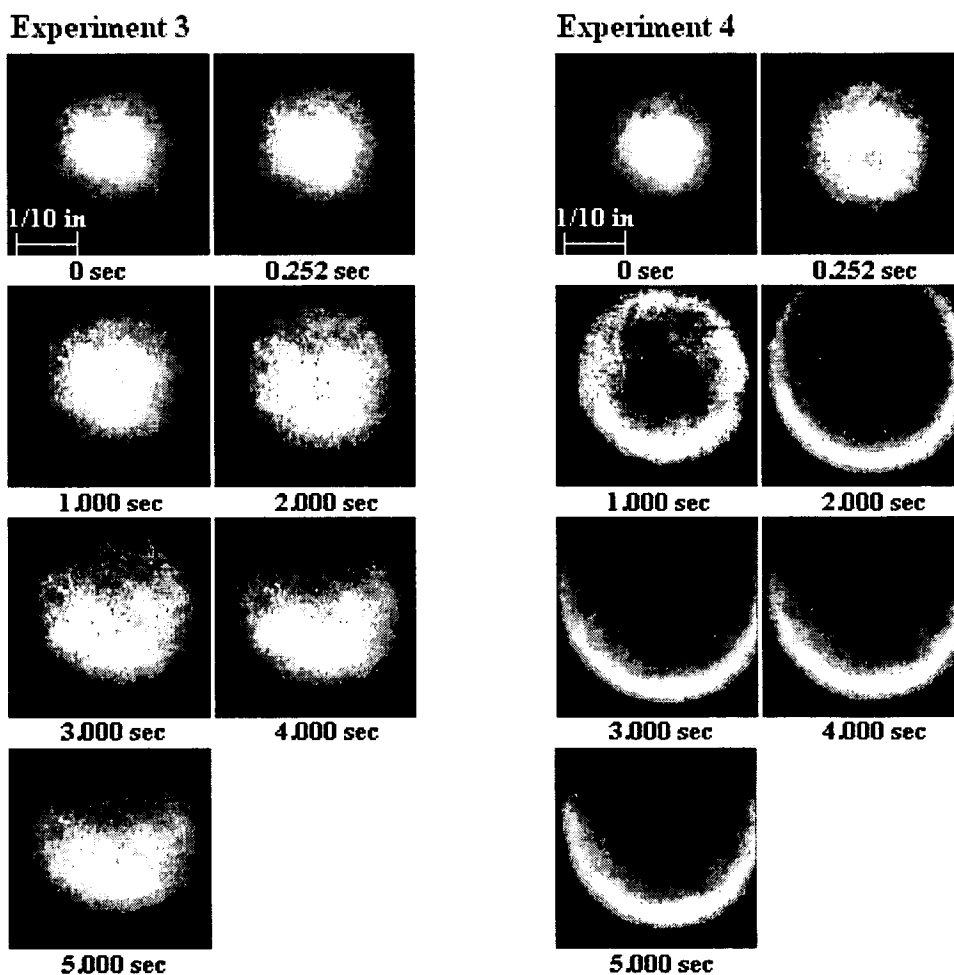


Fig. 6: Results from Experiments 3 and 4 from Table 2. Images are all scaled to the water blanks in Fig. 5. Experiments 3 and 4 had a  $\mu_a$  of  $0.95 \text{ cm}^{-1}$  with a power before the sample of 128 mW and 434 mW respectively.

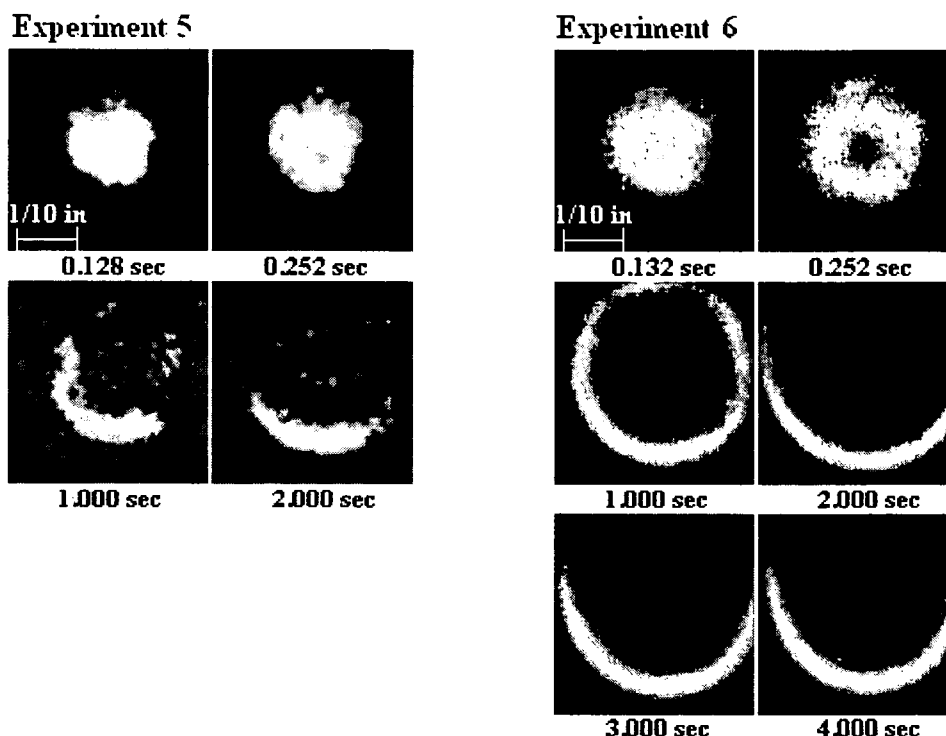


Fig. 7: Results from Experiments 5 and 6 from Table 2. Images are all scaled to the water blanks in Fig. 5. The images here in Experiment 5 required more post processing due to the lower signal to noise ratio for Experiment 5 compared to all other experiments. Experiments 5 and 6 had a  $\mu_a$  of  $1.37 \text{ cm}^{-1}$  with a power before the sample of 320 mW and 615 mW respectively.

The beam never returned to its original state or symmetry in Experiments 3-7 even after several minutes of CW exposure. The rate of the oscillations appeared to dampen in time.

#### 4. DISCUSSION

In Fig. 6, Experiments 3 and 4 had the same absorption. Experiment 3 was at the lowest power, where the first evidence of the donut shape was approximately one second. In Experiment 4 at the higher power, the donut began to appear in 250 milliseconds. In Fig. 7, Experiment 5 and 6 had the same absorption. Experiment 5 had the lower power and revealed the donut around the 250 millisecond mark. At the higher power in Experiment 6, the donut was already taking hold in the first saved frame at 132 milliseconds. Figures 6 and 7 clearly demonstrate how the thermal lensing effect begins to occur for stronger powers and for media with higher absorption coefficients.

The magnitude of the crescent effect was also related to the parameters of power and absorption. In Experiment 3, the crescent was much slower in its appearance and did not extend deeply throughout the beam's profile where only the upper portion of the beam's profile was dissolved. In Experiments 4, 5 and 6, after the formation of the donut, the left over ring took on the shape of the slivered crescent in a similar pattern to Experiment 3 where the upper portion of the beam's profile only dissolved. An example of the oscillations observed in the crescent state can be seen in Fig. 7, Experiment 6 between 2, 3 and 4 seconds. Upon inspection of those three frames, it is evident of the subtle oscillatory response most likely due to convectional currents in the water media. The crescent and observed oscillations are believed to be related to the pressure at the surface of the water sample, the convectional flow from heating and cooling of the water in the beam's path and changes in density and index of refraction within the water resulting from temperature gradients. Models which simulate thermal lensing in thick, strongly absorbing media such as the eye should consider these observations.

Each experiment indicated a convectational process involving thermal diffusion of the absorptive media. This process is not a new result in thermal lensing studies as it has been reported before in other areas of research.<sup>[13-19]</sup> Given the similarities between water and ocular media as presented in Fig. 1, it is reasonable to predict a strongly absorbed wavelength, such as 1300 nm, would thermally lens inside the eye causing a divergence in the beam's focus on the retina. The spot size of the beam at the retina is dynamically changing creating a much larger than anticipated spot size directly impacting the damage threshold prediction. Complete thermal lensing models of the human eye need to consider these convective, oscillating factors. For experimental validation, a method to measure the spot size as a function of time in an artificial eye would aid in understanding the magnitude of the thermal lens effect in the eye.

## 5. REFERENCES

1. Henderson, R. and K. Schulmeister, *Laser Safety*. 2004, Philadelphia, PA: Institute of Physics Publishing. 132-220.
2. Gordon, J.P., et al., *Long transient effects of lasers with inserted liquid samples*. Journal of Applied Physics, 1965. **36**(3): p. 3-8.
3. Vincelette, R.L., et al. *A comparison of a first-order thermal lensing model to a closed aperture Z-scan for the propagation of light in ocular media*. Proceedings in SPIE, *Optical Interactions with tissue and cells XVII*. 2006. San Jose, CA: International Society for Optical Engineering.
4. Thomas, R.J., et al. *A first order model of thermal lensing of laser propagation in the eye and implications for laser safety*. in *International Laser Safety Conference*. 2005. Marina del Rey, CA: Laser Institute of America.
5. Hale, G.M. and M.R. Querry, *Optical Constants of Water in the 200-nm to 200-um Wavelength Region*. Applied Optics, 1973. **12**(3): p. 555-563.
6. Maher, E.F., *Transmission and absorption coefficients for the ocular media of the Rhesus monkey*, in *SAM-TR-78-32*. 1978, USAF School of Aerospace Medicine. p. 1-104.
7. Zolotarev, V.M., et al., *Dispersion and absorption of liquid water in infra-red and radio-frequency regions*. Optics Communications, 1970. **1**(6): p. 301-302.
8. Irvine, W.M., and James Pollack, *Infrared Optical Properties of Water and Ice Spheres*. Icarus, 1968. **8**(1-3): p. 324-360.
9. Palmer, K.F. and D. Williams, *Optical properties of water in the near infrared*. Journal of the Optical Society of America, 1974. **64**(8): p. 1107-1110.
10. Wieliczka, D.M., S. Weng, and M.R. Querry, *Wedge shaped cell for highly absorbent liquids: infrared optical constants of water*. Applied Optics, 1989. **28**: p. 714-719.
11. Curcio, J. and C.C. Petty, *The near infrared absorption spectrum of liquid water*. Journal of the Optical Society of America, 1951. **41**(5): p. 302-304.
12. Cain, C.P., et al., *Artificial eye for In Vitro experiments of laser light interaction with aqueous media*. Journal of Biomedical Optics, 1997. **2**(1): p. 88-94.
13. Motamedi, M., et al., *Thermal lensing in biologic medium*. IEEE Journal of Quantum Electronics, 1988. **24**(4): p. 693-696.
14. Arakelian, S.M., V.E. Drmoyan, MN. Gerke, T.V. Galstian, *Laser - induced instabilities in anisotropic liquid*. in *SPIE - Nonresonant Laser-Matter Interaction* 1997. Bellingham, WA: The International Society for Optical Engineering.
15. Le Sceller, L., S. Meunier-Guttin-Cluzel, C. Roze, and G. Gouesbet, *Influence of the gravity on thermal lens oscillations - Results of the 23rd ESA parabolic flight campaign*. Microgravity Science and Technology, 1997. **X**(2): p. 113-115.
16. Buffett, C.E., and Michael D. Morris, *Convective effects in thermal lens spectroscopy*. Applied Spectroscopy, 1983. **37**(5): p. 455-458.
17. Enokida, Y., Takafumi Kakudo, and Atsuyuki Suzuki, *Application of laser-induced thermal lens oscillation to concentration measurement in organic solutions*. Journal of Nuclear Science and Technology, 1992. **29**(3): p. 255-262.
18. Gouesbet, G. and J. Maquet, *Examination of an analogy toward the understanding of thermal lens oscillations*. Journal of Thermophysics, 1989. **3**(1): p. 27-32.
19. Alfonso, E.F.S., M. A. Rius Revert, M. C. Garcia Alvarez-Coque, and G. Ramis Ramos, *Reduction of convective low-frequency noise in thermal lens spectrometry*. Applied Spectroscopy, 1990. **44**(9): p. 1501-1507.